Projected Pupil Plane Pattern: an alternative LGS wavefront sensing technique

Huizhe Yang,[*] Nazim A. Bharmal and Richard M. Myers

Centre for Advanced Instrumentation, Department of Physics, University of Durham, South Road, Durham DH1 3LE, UK

ABSTRACT

We have analysed and simulated a novel alternative Laser Guide Star (LGS) configuration termed Projected Pupil Plane Pattern (PPPP), including wavefront sensing and the reconstruction method. A key advantage of this method is that a collimated beam is launched through the telescope primary mirror, therefore the wavefront measurements do not suffer from the effects of focal anisoplanatism. A detailed simulation including the upward wave optics propagation, return path imaging, and linearized wavefront reconstruction has been presented. The conclusions that we draw from the simulation include the optimum pixel number across the pupil $N = 32$, the optimum number of Zernike modes (which is 78), propagation altitudes $h_1 = 10\,\mathrm{km}$ and $h_2 = 20\,\mathrm{km}$ for Rayleigh scattered returns, and the choice for the laser beam modulation (Gaussian beam). We also investigate the effects of turbulence profiles with multiple layers and find that it does not reduce PPPP performance as long as the turbulence layers are below h_1. A signal-to-noise ratio analysis has been given when photon and read noise are introduced. Finally, we compare the PPPP performance with a conventional Shack–Hartmann Wavefront Sensor in an open loop, using Rayleigh LGS or sodium LGS, for 4-m and 10-m telescopes, respectively. For this purpose, we use a full Monte Carlo end-to-end AO simulation tool, *Soapy*. From these results, we confirm that PPPP does not suffer from focus anisoplanatism.

Key words: LGS: PPPP – instrumentation: adaptive optics – methods: numerical.

1 INTRODUCTION

As the size of telescopes increases, the correction for atmospheric turbulence using Adaptive Optics (AO) becomes more critical to achieve diffraction-limited performance. Laser Guide Stars (LGSs) are commonly used to sense the distortion of an optical beam travelling in the Earth's atmosphere without the need for a bright, natural reference source. There are two varieties of LGSs, termed Rayleigh and Sodium LGSs. A Rayleigh LGS is created by propagating a beam into the atmosphere and observing the light backscattered from molecules in the atmosphere. As the atmospheric air pressure decreases with altitude, the scattered return also decreases, which limits the altitude of Rayleigh LGS to around 20–25 km (Thompson 1992). More commonly, LGSs are created using a sodium laser which is used to excite sodium atoms in the mesospheric sodium layer (around 90 km) causing them to emit light. For both types of LGSs, especially Rayleigh LGSs, a main difficulty is that for high-altitude turbulence layers, the patch of turbulence observed by the LGS will be smaller than that observed by the astronomical scientific target due to the finite LGS altitude. This so-called focus anisoplanatism becomes more pronounced for larger telescope di-

ameters, such as the proposed next-generation optical ground-based extremely large telescopes (ELTs) with primary mirror diameters of over 30 m. The wavefront error (WFE) caused by focus anisoplanatism can reach ∼155 nm rms (root mean square) on the 10-m Keck telescope, Hawaii, US (Bouchez 2004), and over 300 nm for ELTs.

Laser tomography AO (LTAO) has been developed to mitigate the LGS focus anisoplanatism. Here, several LGSs are generated simultaneously at different positions in the sky. Each LGS is associated with a dedicated wavefront sensor (WFS), and measurements from all WFSs are combined to estimate the 3D turbulence. Take the Keck 10-m telescope as an example again, if seven guide stars are used, the focus-anisoplanatism error can be reduced to ∼50 nm rms (Gavel 2007). According to Hardy (1988), the WFE caused by focus anisoplanatism can be reduced to $(1/N_{\mathrm{LGS}})^{5/6}$ (where N_{LGS} is the number of LGSs) by using multiple LGSs. However the LTAO complexity and expense scale with the number of LGSs used.

Here, we adopt a new alternative LGS configuration proposed by Buscher, Love & Myers (2002) called Projected Pupil Plane Pattern (PPPP) and its associated wavefront sensing method. The key features of PPPP are that a parallel laser beam is projected from the full primary aperture and that sensing takes place on the upward path. The method relies on an observable modulation of the scattered intensity by turbulence-induced phase distortions during upward

[*] E-mail: huizhe.yang@durham.ac.uk

propagation of the laser beam. Compared to LTAO, PPPP does not require multiple LGSs. In addition, as a broad collimated laser beam is projected instead of a focused LGS, the safety hazards for aircraft and satellite are reduced significantly. Similar scheme can also be used for cophasing across segment gaps for large telescopes with primary mirrors based on an assembly of a few large segments, such as the Giant Magellan Telescope (Tuthill 2016).

In this paper, we demonstrate the feasibility of the PPPP method and investigate its performance under different conditions on the 4-m William Herschel Telescope (WHT), La Palma. In Section 2, we introduce the PPPP theory and analyse the signal in the spatial-frequency domain and the high-order effect due to the non-linearities from linearization of TIE (transport-of-intensity equation) and TWE (transport-of-wavefront equation). In Section 3, we present the PPPP simulation modelling including the upward wave optics propagation, return path imaging, and linearized wavefront reconstruction. In Section 4, we present the performance in terms of different PPPP parameters and provide a suitable choice for these parameters. We also analyse different turbulence profiles and provide a signal-to-noise ratio (SNR) analysis when photon and read noise are added. In addition, we compare the performance of PPPP and Shack–Hartmann (SH) WFSs with Rayleigh and sodium LGSs for 4-m and 10-m telescopes using an AO simulation tool. In Section 5, we draw our conclusions.

2 PPPP THEORY

Under the paraxial (Fresnel) condition, a slowly varying electromagnetic wave $u(\vec{r}, z) = I^{1/2}(\vec{r}, z) \exp(j\phi)$ (where $I(\vec{r}, z)$ is the intensity and ϕ is turbulence-introduced phase) satisfies

$$(2jk\partial_z + \nabla^2)u(\vec{r}, z) = 0, \tag{1}$$

where $\partial_z = \partial/\partial_z$, $k = 2\pi/\lambda$ is the wavenumber, and $\nabla^2 = \partial_x^2 + \partial_y^2$. Equation (1) is equivalent to the following pair of equations for the intensity I and phase ϕ,

$$k\partial_z I = -\nabla \cdot (I\nabla\phi), \tag{2}$$

$$2k\partial_z \phi = -|\nabla\phi|^2 + I^{-1/2}\nabla^2(I^{1/2}). \tag{3}$$

Equation (2) is the TIE and equation (3) is the TWE (Teague 1983). The TIE can be approximated as (Roddier 1988),

$$k\frac{I_2 - I_1}{h_2 - h_1} = -\nabla \cdot (I_0\nabla\phi) = -\nabla I_0 \cdot \nabla\phi - I_0\nabla^2\phi, \tag{4}$$

where I_0, I_1, and I_2 are the intensity patterns at the propagation distances 0, h_1, and h_2 correspondingly. Given I_0, I_1, and I_2, we can retrieve the phase ϕ except piston according to equation (4). The linear reconstruction method we use is proposed by Gureyev and Nugent (1996) (see Section 3.3).

The basic set-up for PPPP is illustrated in Fig. 1. A laser beam is expanded to fill the pupil of the telescope and propagates as a collimated beam upwards through the atmosphere. When the laser pulse reaches an altitude of h_1, a snapshot of the Rayleigh backscattered radiation is taken with a camera conjugate at h_1, which will show a disc of illumination corresponding to the telescope pupil (i.e. I_1). When the pulse reaches an altitude of h_2, a second snapshot is taken with a camera conjugate at h_2 (perhaps using the same camera with optical modulation between the two planes as in a curvature WFS set-up). With the obtained I_1 and I_2, we can retrieve the turbulence phase ϕ.
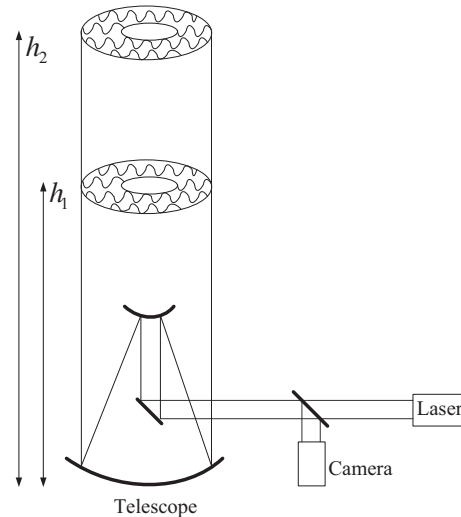

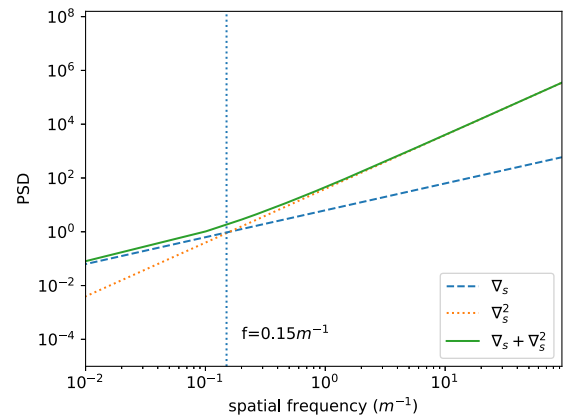**Figure 1.** Schematic diagram of PPPP.

Figure 2. This is the PSD of $\nabla\phi$, $\nabla^2\phi$, and $\nabla\phi + \nabla^2\phi$. ϕ is a sine wave. The cross-over is around 0.15 m^{-1}, which represents $\sim$6.6 m in spatial domain.

2.1 PPPP signal

From equation (4), it is easy to note that the PPPP signal ($I_2 - I_1$) is proportional to $h_2 - h_1$ and the wavelength of the laser. Moreover, the magnitude of $\nabla I_0 \cdot \nabla\phi$ and $I_0\nabla^2\phi$ determines the PPPP signal. Now let us analyse the relative importance of these two terms on the right-hand side of equation (4). We perform a Fourier transform on $\nabla I_0 \cdot \nabla\phi$ and $I_0\nabla^2\phi$ to analyse their relative importance in the spatial-frequency domain. $\mathcal{F}(\nabla I_0 \cdot \nabla\phi)$ equals $\mathcal{F}(\nabla I_0) * \mathcal{F}(\nabla\phi)$ and $\mathcal{F}(I_0\nabla^2\phi)$ equals $\mathcal{F}(I_0) * \mathcal{F}(\nabla^2\phi)$ ($*$ represents convolution). According to the Gureyev and Nugent (1996) linear reconstruction, I_0 is slowly changing inside a finite illuminated aperture Ω and smoothly approaching zero on the boundary Γ. Here, we utilize a Gaussian-like laser beam as I_0 (see Section 3.4). In this case, $\mathcal{F}(\nabla I_0)$ and $\mathcal{F}(I_0)$ are very narrow Gaussian functions and on a similar magnitude level for this Gaussian-like I_0, thus we can neglect these terms and only consider the magnitude of $\mathcal{F}(\nabla\phi)$ and $\mathcal{F}(\nabla^2\phi)$. We analyse two kinds of ϕ: first, a pure sine wave of different spatial frequencies with unit magnitude; then the atmospheric turbulence phases. Fig. 2 shows the power spectral density (PSD) of a sine wave's first and second derivatives. Now we analyse more realistic turbulence phases. Assume that the PSD of the turbulence phase ϕ
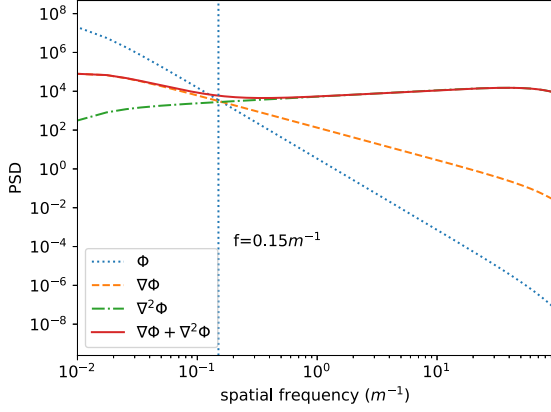
Figure 3. This is the PSD of ϕ, $\nabla\phi$, $\nabla^2\phi$, and $\nabla\phi + \nabla^2\phi$ at $r_0 = 0.15\,\mathrm{m}$ for turbulence phase ϕ. The minimum and maximum spatial frequencies correspond to the outer scale $L_0 = 100\,\mathrm{m}$ and inner scale $l_0 = 0.01\,\mathrm{m}$. We can see that for a very low spatial frequency $f < 0.15\mathrm{m}^{-1}$ (equivalent to 6.6 m in spatial domain), $\nabla\phi$ is more significant than $\nabla^2\phi$, while for higher spatial frequency vice versa.

follows the modified von Kármán PSD (Schmidt 2010),

$$\Phi(f) = 0.023 r_0^{-5/3} \frac{\exp(-f^2/f_m^2)}{(f^2 + f_0^2)^{11/6}}, \tag{5}$$

where r_0 is the atmospheric coherence length, f is the spatial frequency (1/m), $f_0 = 1/L_0$ and $f_m = 5.92/(2\pi l_0)$ (L_0 is the outer scale and l_0 is the inner scale). Then we can obtain the PSD of $\nabla\phi$ and $\nabla^2\phi$ (see Fig. 3),

$$|\mathcal{F}(\phi)|^2 = 0.023 r_0^{-5/3} \frac{\exp(-f^2/f_m^2)}{(f^2 + f_0^2)^{11/6}},$$

$$|\mathcal{F}(\nabla\phi)_{x,y}|^2 = 0.023 r_0^{-5/3} \frac{\exp(-f^2/f_m^2)}{(f^2 + f_0^2)^{11/6}} (2\pi f_{x,y})^2,$$

$$|\mathcal{F}(\nabla^2\phi)|^2 = 0.023 r_0^{-5/3} \frac{\exp(-f^2/f_m^2)}{(f^2 + f_0^2)^{11/6}} (2\pi f)^4. \tag{6}$$

For a Shack–Hartmann WFS, the slope of the phase $\nabla\phi$ is the measured signal, while for PPPP both $\nabla\phi$ and $\nabla^2\phi$ contribute to the needed signal. Fig. 3 shows that $\nabla\phi$ decreases with the spatial frequency and $\nabla^2\phi$ on the contrary increases with the spatial frequency. The sum of $\nabla\phi$ and $\nabla^2\phi$ keeps almost constant across the spatial frequency domain. Therefore, the PPPP signal is almost independent of the spatial frequency for this Gaussian-like laser beam.

Notably, here the PPPP signal is actually the on-sky measurement without considering the return path. Given a certain pixel size of the detector as shown in Section 3.2, the effect of the return path can be neglected and the high frequencies are limited by the pixel size instead of the turbulence. For instance, if there are 32 pixels across the pupil on a 4-m telescope, then the corresponding cut-off frequency equals $\frac{N/2}{D} = \frac{16}{4\,\mathrm{m}} = 4$ (1/m).

2.2 High-order effect

There are non-linearities due to the linearization of the TIE, as well as the fact that the wavefront is changing as the wave propagates according to equation (3). Milman (1996) and van Dam (2002) have provided detailed analysis of the non-linear effects for a curvature WFS. In this subsection, we will focus on similar effects for PPPP and analyse the condition under which the high-order effect on PPPP
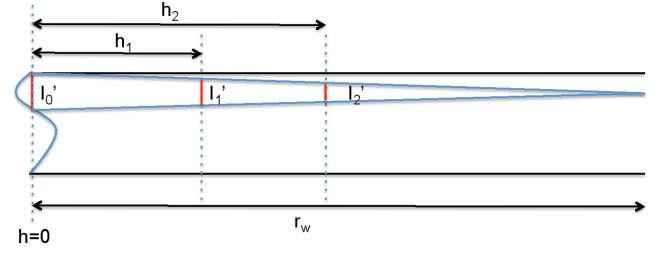
can be neglected. Let the turbulence wavefront at the ground have local curvature $C_w = 1/r_w$ where r_w is the local radius of curvature of the wavefront over a small area with illumination I_0' (see Fig. 4). As the light propagates to h_1 and h_2, the illumination will become I_1' and I_2' and the signal from the equivalent small areas is $I_2' - I_1'$. The following equation gives expressions for I_1', I_2', and $I_2' - I_1'$, which are

$$I_1'\left(\frac{r_w - h_1}{r_w}\right)^2 = I_0',$$

$$I_2'\left(\frac{r_w - h_2}{r_w}\right)^2 = I_0',$$

$$I_2' - I_1' = I_0'\left[\left(\frac{r_w}{r_w - h_2}\right)^2 - \left(\frac{r_w}{r_w - h_1}\right)^2\right]. \tag{7}$$

Expending about h, equation (7) becomes

$$I_2' - I_1' = I_0' \times \left[2\left(\frac{h_2 - h_1}{r_w}\right) - 3\left(\frac{h_2^2 - h_1^2}{r_w^2}\right) + \dots\right], \tag{8}$$

when $r_w \gg h$. The first term in equation (8) corresponds to the curvature of the turbulence phase and the others cause the high-order effect. To limit the high-order effect (here only the first and second terms are considered), we have the following criterion

$$3\left(\frac{h_2^2 - h_1^2}{r_w^2}\right) \ll 2\left(\frac{h_2 - h_1}{r_w}\right), \tag{9}$$

which can be simplified as

$$r_w \gg 1.5(h_1 + h_2). \tag{10}$$

Equation (10) tells us $h_1 + h_2$ should be as small as possible to reduce the high-order effect, however the PPPP signal from equation (4) shows that $h_2 - h_1$ should be, on the contrary, as big as possible. Thus, an optimal choice for h_1 and h_2 should be made. Due to the fact that the Rayleigh beacon can only be detected at an altitude where air density is still high, typically between 10 and 20 km, and the fact that the atmospheric turbulence between h_1 and h_2 can be only sensed by I_2 (see Section 4.2), we adopt the choice that $h_1 = 10\,\mathrm{km}$ and $h_2 = 20\,\mathrm{km}$ for the following simulations.

3 PPPP SIMULATION MODELLING

A PPPP simulation can be divided into three steps: first, to propagate a collimated beam upwards from the telescope pupil plane to several different altitudes (a minimum of two is required) – termed upward propagation; then to reimage the Rayleigh backscattered intensity patterns at those altitudes through the same telescope by cameras conjugate at the corresponding heights – termed return path; finally, to retrieve the distorted phase using the subtraction of the images from these cameras – termed reconstruction. The images have to be scaled to the same flux to satisfy the conservation of

Figure 4. Schematic diagram of PPPP high-order effect.

energy. The major difference between PPPP and conventional LGS wavefront sensing lies in the fact that the required signal for PPPP is generated by the upward propagation of the collimated laser beam. Meanwhile, the return path can be treated simply as a re-imaging process, i.e. a convolution of the atmospheric downward PSF with the backscattered patterns, which may degrade the backscattered patterns depending on the strength of the turbulence. However, for conventional LGS SH wavefront sensing, the return path is responsible for the needed slope measurement while the upward propagation of the focused laser beam just introduces undesired LGS distortion.

For a conventional LGS combined with a SH WFS, a natural star is still required for the tip-tilt correction, since movement of the LGS caused by the uplink propagation is observed by the SH WFS as a tip-tilt aberration. PPPP experiences a similar problem, where the tip-tilt signal generated from the upward propagation (which is a global movement of the intensity pattern) will be affected by the return path, therefore it is also necessary to use a natural star to provide the tip-tilt information. Due to this reason, from now on we only consider the atmospheric aberrations with tip-tilt removed. To keep the comparison between PPPP and SH WFS more simple and compatible, all the simulations are run in an open loop here.

Another unique phenomenon for PPPP is that the telescope primary mirror, which has been used to launch the laser beam, is also used to collect the scattered light from the sky, as well as the light from the scientific object. Thus, if we use a short-wavelength laser, say 589 nm (typical for sodium LGS), and an infrared scientific camera, the fluorescence from the telescope optics could cause interference for the science instrument. Therefore, we have to play it the other way round, using a pulsed laser longer than the imaging wavelength such as Nd:YAG at 1064 nm and limit the science observations to a shorter wavelength. However, to obtain diffraction limited images, one needs a residual rms WFE of about 1/8 times the imaging wavelength or less, which is very challenging for PPPP since the imaging wavelength is restricted to be shorter than the laser wavelength. This difficulty applies to all visible AO systems though, and visible AO is of great interest for particular celestial objects and can provide higher resolution diffraction-limited images.

3.1 Upward propagation

The upward propagation process is performed by a Fresnel diffraction kernel (Schmidt 2010 and Voelz 2011), according to

$$u(x, y; h) = \mathcal{F}^{-1} \left[H(f_x, f_y) \times \mathcal{F}[u(x, y; h = 0)] \right], \quad (11)$$

where $u(x, y; h)$ are the electromagnetic fields at h. $H(f_x, f_y)$ is the transfer function of free-space propagation and equals

$$H(f_x, f_y) = e^{jkh} e^{-j\pi\lambda h(f_x^2 + f_y^2)}, \quad (12)$$

where (f_x, f_y) is the coordinate in the spatial-frequency domain at $h = 0$. The reason we use the transfer function (equation 12) instead of the impulse response is because it is suitable for relatively short propagation distance (Voelz 2011). The critical distance according to Voelz is $\Delta x L / \lambda$ (where Δx is the sample interval in the spatial domain, L is the total extent). To avoid problems with the periodicity of the Fourier transform involved in the propagation simulation, the total extent L is $2 \times D$ according to the Nyquist sampling criteria. So in our case the critical distance equals $4 \text{ m}/32 \times 8 \text{ m}/1.06 \text{ um} \approx 1000 \text{ km}$ if there are 32 pixels across the pupil. This Fresnel diffraction has been performed by two steps. First, $u(x, y; h = 0)$ propagates from the source plane to an intermediate plane; then propagates to the observation plane. In this way, we can control the grid spacing in the observation plane by
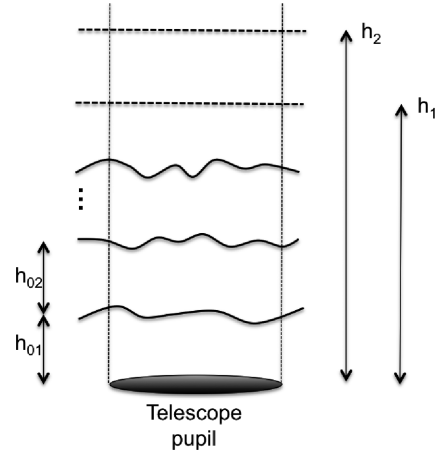

Figure 5. Schematic diagram of upward propagation.

choosing the intermediate plane (Schmidt 2010). The atmospheric turbulence is simplified as several phase screens located at different altitudes generated by the Monte Carlo FT (Fourier transform) method (Schmidt 2010). Given these phase screens, we perform Fresnel diffraction (equation 11) starting from the electromagnetic field at the pupil plane $u(x, y; h = 0)$ to the altitude of the first phase screen h_{01}, obtaining the electromagnetic field $u(x, y; h_{01})$ at h_{01}. Then adding the phase screen ϕ, we perform Fresnel diffraction using $u(x, y; h_{01}) \times \exp(j\phi)$ as the new source and propagate this new source with distance equalling h_{02} (see Fig. 5). This process is repeated until the beam reaches h_1 and h_2, obtaining the intensity patterns I_1 and I_2 at h_1 and h_2. To make the simulation more realistic, we use 256×256 grids across the total extent L for the electromagnetic fields $u(x, y)$ and phase screens, then bin them to 64×64 pixels for I_1 and I_2 (which means 32×32 pixels are used to sample the telescope pupil D for I_1 and I_2 in the detector).

3.2 Return path

Regarding the return path, two issues should be taken into consideration: (1) the amount of flux scattered back (relating to SNR), which can be calculated by the LIDAR (light detection and ranging) equation (Hardy 1988) given the laser power, telescope diameter, etc.; (2) and the downward turbulence-introduced PSF, which is used to convolve with the intensity patterns on sky to perform the re-imaging process.

The LIDAR equation is as follows:

$$N(h) = \left(\frac{E\lambda}{h_P c} \right) (\sigma_B n(h) \Delta h) \left(\frac{A_R}{4\pi h^2} \right) (T_0 T_A^2 \eta), \quad (13)$$

where $N(h)$ is the number of photons scattered back; $\lambda = 1.06$ um; $n(h)$ is the column density of scatterers, which is the atmospheric atoms for Rayleigh scatter and sodium atoms for sodium resonance fluorescence. The number of atmospheric atoms is a function of the atmospheric pressure and temperature, which are both determined by the altitude h. The numbers of atmospheric atoms per cubic metre at h_1 and h_2 are $n(10 \text{ km}) \approx 1.00 \times 10^{25} \text{ m}^{-3}$ and $n(20 \text{ km}) \approx 3.18 \times 10^{24} \text{ m}^{-3}$. The sodium atom density is approximately $5 \times 10^9 \text{ m}^{-3}$ and its depth is 10 km.

In equation (13), σ_B is the effective backscatter cross-section, which is equal to (Hardy 1988)

$$\sigma_B^R = 5.45 \times 10^{-32} [550/\lambda(\text{nm})]^4 \quad \text{Rayleigh scattering,}$$
$$\sigma_B^S = 4 \times 10^{-16} (\text{at } 589 \text{ nm}) \quad \text{sodium fluorescence.} \quad (14)$$

Table 1. Parameters of the LIDAR equation. D is the diameter of the telescope primary mirror ($A_R = 12.56\,\text{m}^2$); h_P is the Planck's constant; c is the velocity of light; η is the quantum efficiency of photon detector at wavelength λ; T_0 is the transmission of the optical components and T_A is the one-way transmission of the atmosphere; E is the laser energy during the exposure time (2.5 ms), here an average 20 W pulsed laser with a 5 KHz frequency is used. So $E = 20\,\text{W}/5\,\text{KHz} \times 2.5\,\text{ms} \times 5\,\text{KHz} = 0.05\,\text{J}$; Δh_1 and Δh_2 are the range gate depth for h_1 and h_2, respectively (it has been proven in Section 4.3 that photon noise mainly comes from the detector conjugate at h_2, so increasing Δh_2 can improve SNR significantly).

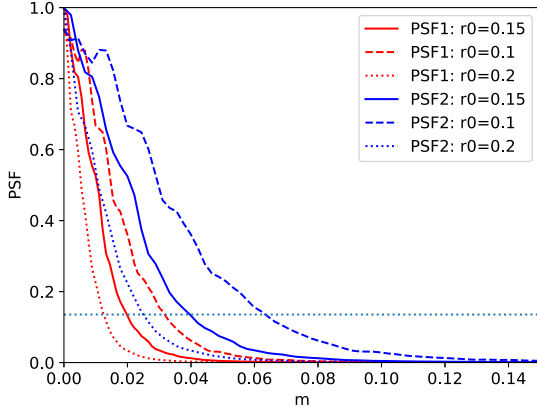| $D = 4\,\text{m}$	$h_P = 6.626 \times 10^{-34}\,\text{J s}$	$c = 3 \times 10^8\,\text{m s}^{-1}$
$\eta = 0.8$	$T_0 = 0.5$	$T_A = 1\text{M}$
$E = 0.05\,\text{J}$	$\Delta h_1 = 1\,\text{km}$	$\Delta h_2 = 5\,\text{km}$

Figure 6. Return-path turbulence-introduced averaged PSF projected to the object plane from 500 random phase screens with different r_0. PSF1 and PSF2 are corresponding to h_1 and h_2.

The other parameters in the LIDAR equation are listed in Table 1. If $h_1 = 10\,\text{km}$ and $h_2 = 20\,\text{km}$, and $\Delta h_1 = 1\,\text{km}$ and $\Delta h_2 = 5\,\text{km}$, the numbers of photons scattered back are 4.24×10^4 and 1.67×10^4, respectively. Notably, here Δh_2 is 5 times Δh_1 since most of the noise comes from h_2, and increasing Δh_2 can improve the SNR significantly. The expected flux return for sodium laser is 1.46×10^5 (at 589 nm).

The downward turbulence-introduced PSF can be obtained by the scaled Fourier transform of the generalized pupil $P(x, y) = I_0^{1/2} \exp(j\phi)$ according to the following equation (Goodman 1996):

$$\text{PSF} = |\mathcal{F}[P(\lambda h f_x, \lambda h f_y)]|^2. \tag{15}$$

The averaged return-path PSFs for h_1 and h_2 projected to the sky for different r_0 are shown in Fig. 6. To reduce the effect of the atmospheric PSF on the PPPP signal, we have to limit the PSF width ($1/e^2$ width here) to one pixel or less. From Fig. 6 the width of PSF2 is nearly twice that of PSF1, which means the intensity pattern at h_2 is more blurred than h_1 during the return path. Considering the worse case, i.e. PSF2, the PSF2 width for $r_0 = 0.15\,\text{m}$ (at 500 nm) is approximately $0.04 \times 2 = 0.08\,\text{m}$. If the PSF is one pixel or less, then the required pixel number N should be at most $D/0.08 = 50$ for a 4-m telescope. If the telescope primary mirror D is doubled, then the maximum pixel number N can be doubled as well. For $r_0 = 0.1$ and 0.2 m, the maximum N are 30 and 80, respectively. During the return path the laser speckle pattern, produced by the diffuse reflections of laser light acting on the atmosphere, can be ignored since the time-scale of atmospheric molecules moving

($\sim$ several ns) is much smaller than the time-scale of the turbulence changing ($\sim$ several ms), and the laser speckle will be averaged out.

3.3 Reconstruction

The reconstruction process is based on the Gureyev and Nugent (1996) linear method. Here, we briefly recall the Gureyev and Nugent linear reconstruction method. First, let us calculate the scalar product of equation (4) with Zernike polynomials, the scalar product of the left-hand side equals

$$\left\langle k \frac{I_2 - I_1}{h_2 - h_1}, Z_j \right\rangle = R^{-2} \int_0^{2\pi} \int_0^R k \frac{I_2 - I_1}{h_2 - h_1} \cdot Z_j r \, dr \, d\theta, \tag{16}$$

where Z_j is the j-th Zernike polynomial, and R is the radius of the telescope primary mirror. We define $F_j = <k(I_2 - I_1)/(h_2 - h_1), Z_j>$. On the other hand, the scalar product of the right-hand side of equation (4) is

$$\left\langle -\nabla \cdot (I_0 \nabla \phi), Z_j \right\rangle = R^{-2} \int_0^{2\pi} \int_0^R -\nabla \cdot (I_0 \nabla \phi) Z_j r \, dr \, d\theta. \tag{17}$$

If we decompose the turbulence phase ϕ into Zernike polynomials, then

$$\phi = \sum_{i=2}^P a_i Z_i, \tag{18}$$

where a_i is the coefficient of the i-th Zernike polynomial and P is the highest order Zernike term used. Substituting equation (18) into equation (17), we get

$$\left\langle -\nabla \cdot (I_0 \nabla \phi), Z_j \right\rangle = \sum_{i=2}^P a_i R^{-2} \int_0^{2\pi} \int_0^R -\nabla \cdot (I_0 \nabla Z_i) Z_j r \, dr \, d\theta. \tag{19}$$

Using integration by parts $\int u \, dv = uv - \int v \, du$, equation (19) can be written as

$$\left\langle -\nabla \cdot (I_0 \nabla \phi), Z_j \right\rangle = \sum_{i=2}^P a_i R^{-2} \int_0^{2\pi} \int_0^R I_0 \nabla Z_i \cdot \nabla Z_j r \, dr \, d\theta, \tag{20}$$

if the intensity distribution I_0 satisfies

$$I_0 > 0 \quad \text{inside the finite illuminated aperture } \Omega,$$
$$I_0 = 0 \quad \text{outside } \Omega \text{ and on the boundary } \Gamma, \tag{21}$$

thus the integral over the boundary Γ disappears. Now it is convenient to introduce the matrix $\mathbf{M}$ with elements

$$M_{ij} = \int_0^{2\pi} \int_0^R I_0 \nabla Z_i \cdot \nabla Z_j r \, dr \, d\theta. \tag{22}$$

Using this definition, we can rewrite equations (16) and (20) as a system of algebraic equations for the unknown Zernike coefficients

$$R^2 F_j = \sum_{i=2}^P M_{ij} a_i \quad \text{or} \quad R^2 \mathbf{F} = \mathbf{Ma}. \tag{23}$$

Finally, to retrieve the phase ϕ, we simply need to find the Zernike coefficients a_i, which equals

$$\mathbf{a} = R^2 \mathbf{M}^{-1} \mathbf{F}. \tag{24}$$

Equation (24) is the final expression for this linear reconstruction. $\mathbf{F}$ is based on the measured signal and the matrix $\mathbf{M}$ can be theoretically calculated given the intensity distribution I_0.
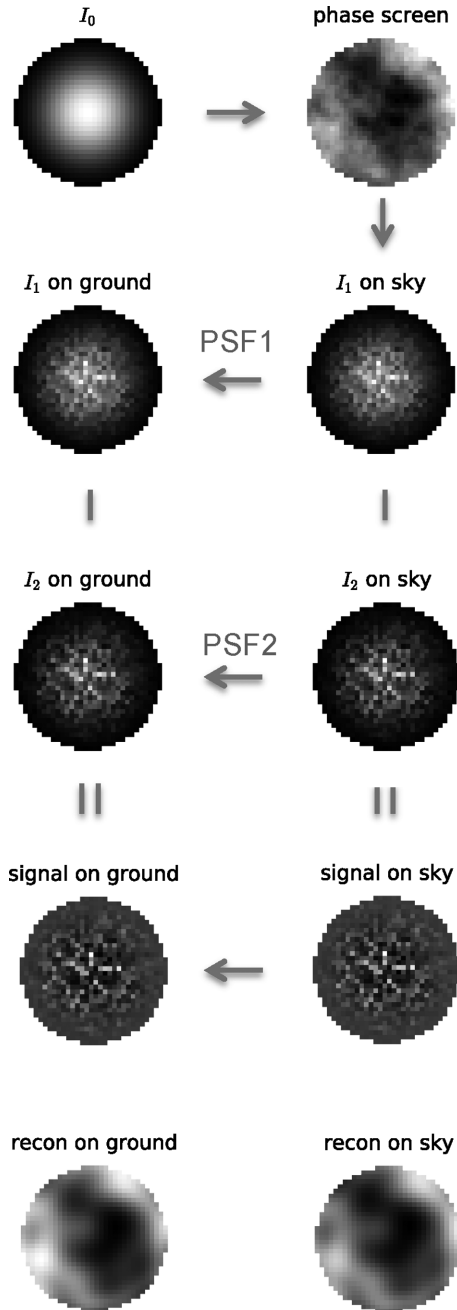
Figure 7. An example of PPPP simulation process, including upward propagation, return path, and reconstruction.
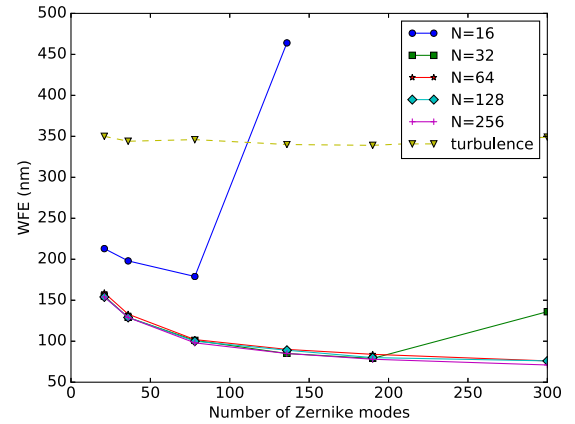

Figure 8. Investigation of the number of pixels N and the number of Zernike modes. The turbulence WFE represents the rms of the input phase screens (around 350 nm when $r_0 = 0.15$ m at 500 nm). The result is an average of 100 random phase screens and the same for the other results in this section.

is on the ground). I_1 and I_2 on sky are then convolved with the atmosphere downward PSF1 and PSF2, respectively, generated by the same phase screen, forming I_1 and I_2 on the ground. It is worth mentioning that I_1 and I_2 have been normalized to the same flux amount (here, normalized to the total amount of photons scattered back from h_2 before subtraction). The reconstructed phases (at the last line in Fig. 7) show great similarity to the input phase screen albeit at a lower resolution.

4 PPPP PERFORMANCE ANALYSIS

In this section, we provide apt choices for PPPP parameters. We also analyse the effect of the turbulence profiles (including the altitudes and strengths of the turbulence layers) and provide a detailed SNR analysis when photon and read noise are added. Finally, we compare the PPPP performance with the SH WFS using Rayleigh and sodium LGSs for 4-m and 10-m telescopes.

4.1 Choosing suitable PPPP parameters

In this subsection, we analyse the PPPP performance given different parameters and determine suitable choices for the pixel number, the number of Zernike modes, h_1 and h_2, etc. The PPPP performance is estimated by the residual WFE between the input phase screen and the reconstructed phase.

4.1.1 Investigation of the number of pixels and Zernike modes

Fig. 8 shows the residual WFE between the reconstructed phase and the input phase screen and the rms of the input phase screen (without tip–tilt) in terms of different pixel number N across the pupil in the detector and the number of Zernike modes. Except $N = 16$, we find that the residual WFE shares a similar tendency when N changes from 32 to 256, where the WFE declines from 21 to 78 Zernike modes, followed by a slower decrease from 78 to 300 Zernike modes (apart from a sudden increase at 300 Zernike modes when $N = 32$). That indicates optimal choices for N and Zernike modes are 32 and 78, respectively, considering the balance of the complexity and the performance.
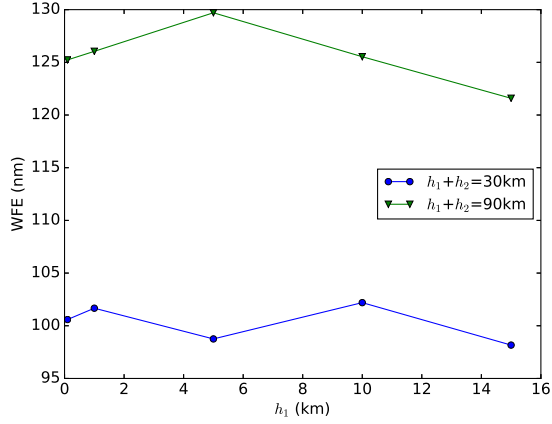
3.4 An example of PPPP simulation process

Fig. 7 shows an example of a complete PPPP simulation process for a 4-m telescope. Here, a Gaussian-like beam

$$I_0 = a + \exp\left[-(x^2 + y^2)/(2\sigma^2)\right], \tag{25}$$

with $a = -0.1297$ and $\sigma = 1.05$ m has been used. In this way, the input laser beam satisfies equation (21). The choice of $\sigma = 1.05$ m is to guarantee that I_0 is smoothly approaching zero on the boundary and the effective sensing area (the bright area of I_0) can be as big as possible. As shown in Fig. 7, the laser beam propagates to h_1 and h_2, forming I_1 and I_2 on sky, after passing through a random phase screen (with tip–tilt removed and assuming the phase screen

Figure 9. Investigation of the propagation heights h_1 and h_2. This figure is consistent with the theoretical analysis in Section 2.2, where PPPP performance is inversely proportional to $h_1 + h_2$.

Table 2. PPPP parameters for WHT.

$D = 4$ m	$\lambda = 1.06$ um	$N = 32$	78 Zernike modes
$h_1 = 10$ km	$h_2 = 20$ km		Gaussian-like I_0

4.1.2 Investigation of h_1 and h_2

Regarding the propagation heights h_1 and h_2, Fig. 9 shows that the PPPP performance is similar when $h_1 + h_2$ is constant and it gets worse when $h_1 + h_2$ increases due to the high-order effect (see Section 2.2). This proves again that $h_1 + h_2$ should be as small as possible. Considering the balance of the high-order effect and the PPPP sensitivity, the combination of $h_1 = 10$ km and $h_2 = 20$ km is chosen.

4.1.3 Investigation of the intensity distribution I_0

Another variable parameter for PPPP is the intensity distribution I_0 at the telescope pupil. To investigate that, $I_0 = 1$ inside the pupil Ω (like a top-hat) has been adopted and the corresponding averaged WFE is around 160 nm rms. For the Gaussian-like beam the residual WFE is around 100 nm rms. This is because the top-hat beam does not meet equation (21) (not smoothly approaching 0 on the boundary), hence not quite applicable for this linear reconstruction. Therefore, we come to the conclusion that a Gaussian-like beam is a better option.

Now we have analysed the effects of the pixel number across the pupil, the number of Zernike modes, the propagation heights h_1 and h_2, and the intensity distribution I_0. A reasonable choice for the PPPP simulation parameters on the WHT is shown in Table 2.

4.2 Investigation of turbulence profile

Until now, only one turbulence layer on the ground has been taken into consideration, however, the real turbulence profiles are never like that. In this subsection, we first look into one turbulence layer at different altitudes and then analyse multiple turbulence layers located at different altitudes.

As shown in Fig. 10, when the turbulence layer is below $h_1 = 10$ km, the WFE is nearly constant. This can be proven by equation (4), where the signal $I_2 - I_1$ only relates to $h_2 - h_1$. However, when the turbulence layer h is in between h_1 and h_2, only the intensity pattern at h_2 can see the turbulence and, of course when
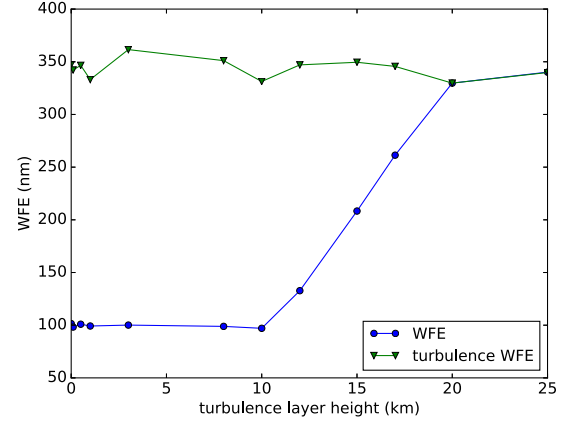

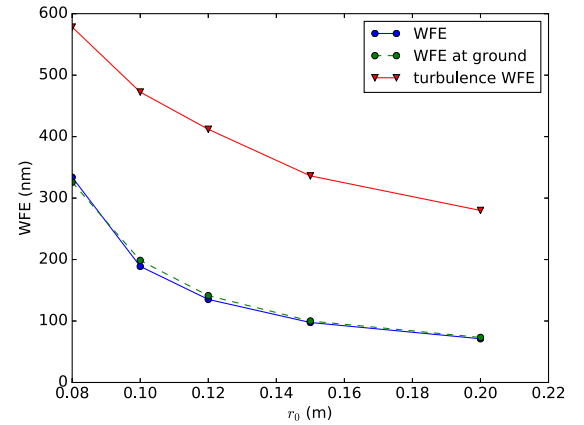**Figure 10.** One turbulence layer at different altitudes.

Figure 11. Three turbulence layers at different altitudes ('WFE' curve) with different r_0, compared with one compact turbulence layer (sum of these three turbulence layers) at ground ('WFE at ground' curve).

$h > h_2$, PPPP is blind to its effect. Fortunately, if the AO system operates in a closed loop, the turbulence between 10 and 20 km can be much better compensated to nearly the level when the turbulence is below 10 km. Here, we only consider an open-loop system as the emphasis of this paper is to introduce this novel alternative LGS wavefront sensing technique instead of the point of view of a complete AO system. An example of three turbulence layers, located at $[0, 5, 10]$ km with relative strength $[0.5, 0.3, 0.2]$, is shown in Fig. 11, compared with a compact turbulence layer (sum of these three turbulence layers) on the ground. From this figure, we know that multiple turbulence layers should not reduce PPPP performance as long as the turbulence layers are below h_1.

4.3 Investigation of SNR

Until now, all the simulation and analysis are based on a noise-free situation. In this subsection, we present a detailed SNR analysis when the photon and read noise are added. First, we consider the photon noise. Assume the normalized signal is $s_n = I_2 - I_1/2I_0$, then the variance of the error is approximated as follows according to van Dam (2002),

$$E[(s_n - \overline{s_n})^2] \approx 1/(2N_{\text{photon}}), \tag{26}$$

where N_{photon} is the average number of photons in each pixel over the pupil. If 32×32 pixels are used in the detectors to sample the
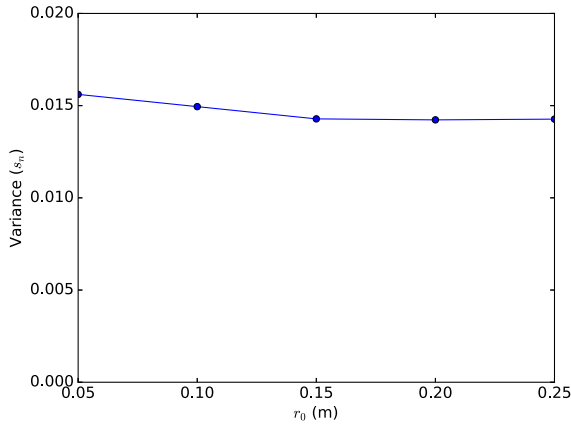
Figure 12. Variance of the error in the estimate of s_n with different r_0. The results are an average of 20 random phase screens and for each phase screen 20 random Poisson distributions are performed to average the photon noise. The same applies to other figures in Section 4.3.
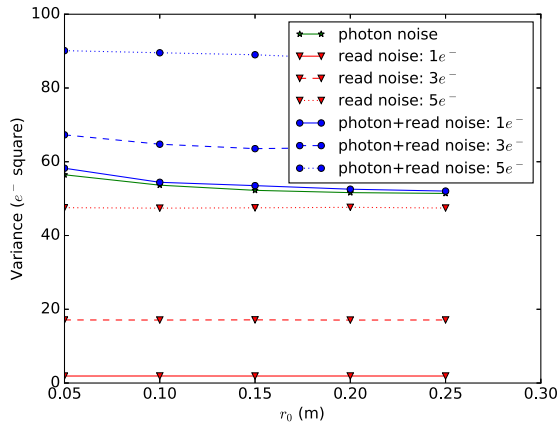

Figure 13. Variance of the error in terms of photon noise, read noise to a different degree and their combination. The variance of the read noise is 2 times the theoretical value since for PPPP two detectors are used together.
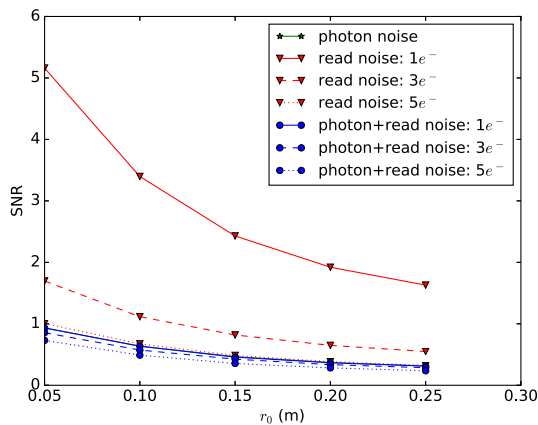

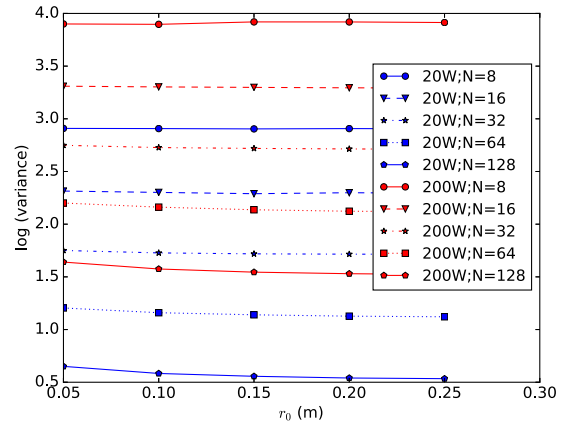**Figure 14.** SNR including photon noise, read noise to a different degree and their combination.

Figure 15. Log value of variance of photon noise with different pixel numbers and laser powers.
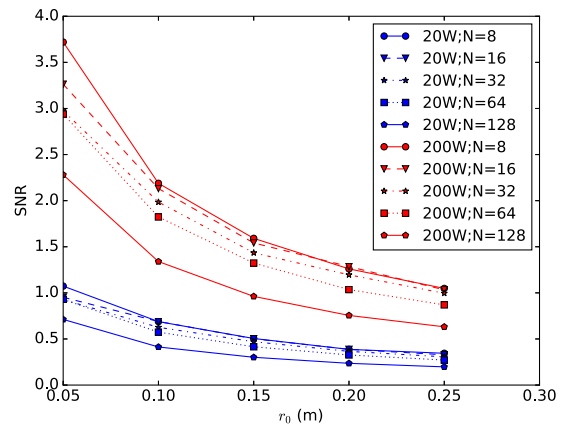

Figure 16. SNR including only photon noise with different pixel numbers and laser powers.

pupil, the average return fluxes in each pixel of detectors conjugate at h_1 and h_2 are 76 and 30 photons, respectively. Then the theoretical variance of the error caused by photon noise according to equation (26) should be $1/(2 \times 76) = 0.0066$ and $1/(2 \times 30) = 0.0167$. The average variance of s_n with different r_0 is plotted in Fig. 12, where $s_n \approx 0.015$ for each pixel. It can be seen that the curve exhibits the behaviour predicted by equation (26) more closely when the amount of return flux from h_2 is used. That means the photon noise for PPPP comes mainly from the detector conjugate at h_2.

Now we add read noise as well to analyse the noise variance and the SNR. Assume the signal $s = I_2 - I_1$, then the variance of the error is rms of $(E[(s - \bar{s})^2])$ over all pixels and the signal is $\sqrt{(\text{rms}(s^2))}$. Fig. 13 shows the variance of the noise including the photon noise and read noise, as well as their sum. It can be seen that both photon and read noise are independent of the turbulence strength r_0, and photon noise is dominant until read noise equals $5e^-$ rms. Fig. 14 provides the corresponding SNR with the same kinds of noise shown in Fig. 13 in terms of different r_0. It is obvious that all SNR curves decrease as r_0 increases, which demonstrates that PPPP signal is inversely proportional to r_0. This is fairly easy to understand from equation (4), where the signal $I_2 - I_1$ is proportional to ϕ. Again from Fig. 14, we find that photon noise is the main limit to SNR when read noise is less than $5e^-$. In reality, we intend to adopt an Avalanche PhotoDiode detector instead of a CCD to reduce the read noise to nearly 0. Now if we ignore read noise and analyse the effect
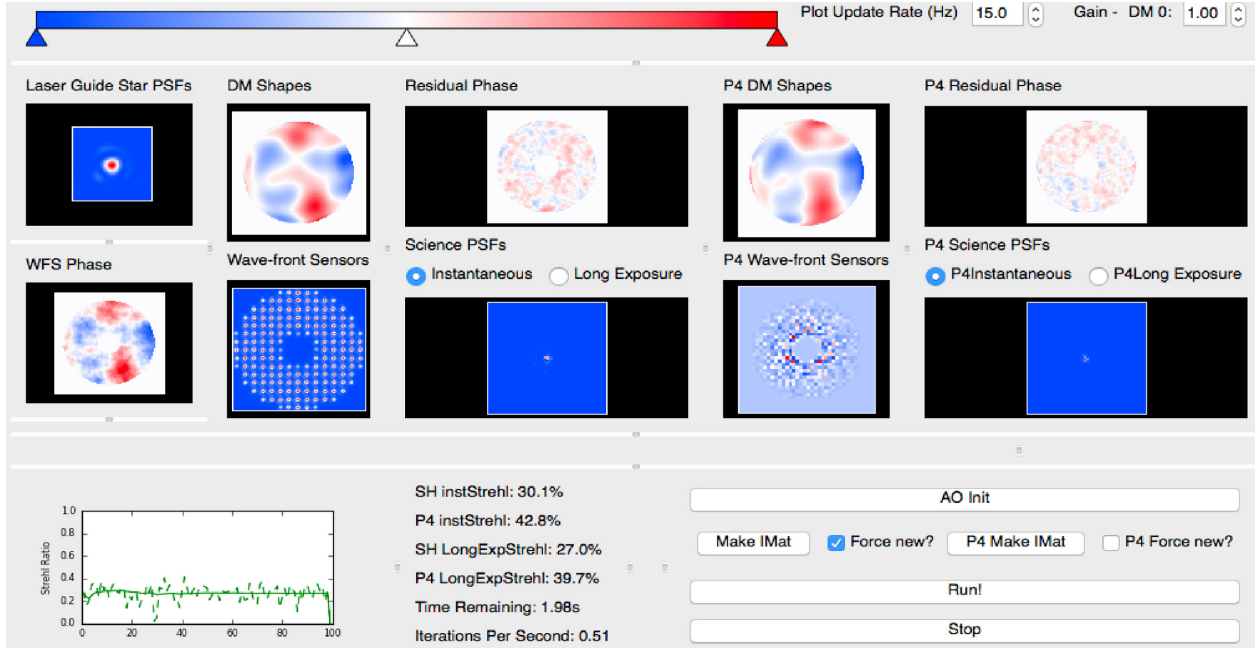
Figure 17. *Soapy* GUI including PPPP model.

Table 3. Parameters for *Soapy* simulation platform. PPPP and Shack–Hartmann share the same parameters for telescope, atmosphere, DM, and science camera. T_0 is the transmission of the optical components and T_A is the one-way transmission of the atmosphere.

Telescope	Atmosphere	DM	Science camera
$D = 4\,\text{m}$ or $10\,\text{m}$	$r_0 = 0.15\,\text{m}$ (at $500\,\text{nm}$)	Zernike DM	$\lambda = 0.8\,\text{um}$
128×128 pixels over pupil	$T_A = 1$	78 Zernike modes	64×64 pixels
$T_0 = 0.5$			
PPPP		**Shack–Hartmann WFS**	
32×32 (or 80×80) pixels	$\lambda = 1.06\,\text{um}$	LGS height: 10 or 20 or 90 km	$\lambda = 1.06\,\text{um}$ (or $589\,\text{nm}$)
$h_1 = 10\,\text{km}$	$h_2 = 20\,\text{km}$	15×15 sub-apertures	Pixels per subap: 14×14
Δh_1: $1\,\text{km}$	Δh_2: $5\,\text{km}$	FOV per subap: 5.5 arcsec	Laser launch pupil: $0.3\,\text{m}$
read noise $3e^-$	$\eta = 0.8$	read noise $3e^-$	

of return flux on photon noise, we find that the variance of photon noise is proportional to the flux amount in each pixel from Fig. 15. The number of photons in each pixel can be determined either by the laser power or the pixel size in a similar manner. The corresponding SNR is shown in Fig. 16, where we can come to the conclusion that binning the images (increasing the pixel size) to increase photon number in each pixel can improve SNR very slightly compared to increasing the laser power. That is because the binned signal is very badly sampled.

There are other noise sources such as dark current and sky background. These two kinds of noises are normally very small compared to photon and read noise. For example, the dark current is around $0.015\,e^-$ during 2.5 ms exposure time for the Keck OSIRIS (a near-infrared integral field spectrograph) detector. According to Gemini tests on Mauna Kea, the sky background is only about 10 photons per second per arcsec squared per metre squared for $\lambda = 1.06\,\text{um}$.

4.4 Comparison with Shack–Hartmann WFS

The PPPP simulation model has been integrated into *Soapy*, which is a Monte Carlo AO simulation written in the Python programming language (Reeves 2015). The simulation is arranged into objects which represent individual AO components, such as the atmosphere, WFS, DM, reconstruction, etc. A GUI of *Soapy* including PPPP model is shown in Fig. 17.

To demonstrate the performance of PPPP for 4-m and 10-m telescopes, a conventional SH WFS with a Rayleigh LGS focused at 10 or 20 km, or a sodium LGS has been used as a comparison, with the parameters listed in Table 3. Fig. 18 shows the performance of the PPPP and SH with Rayleigh LGS (10 and 20 km) and sodium LGS when the turbulence layer is located at 0, 5, and 10 km, respectively. Looking at the SH curves with Rayleigh and sodium LGSs (blue, green, and red curves), it is obvious that when the turbulence layer is on the ground, the WFEs for Rayleigh LGSs focused at 10 and 20 km are very similar. The small difference between sodium LGS and Rayleigh LGSs in this case is caused by different wavelengths used (1.06 um for Rayleigh LGSs and 589 nm for sodium LGS). However, when the turbulence layer is located at 5 or 10 km, sodium LGS gives much better performance than Rayleigh LGSs. That proves the existence of focus anisoplanatism for a single LGS SH. According to the propagation of error for uncorrelated variables with equal weight,

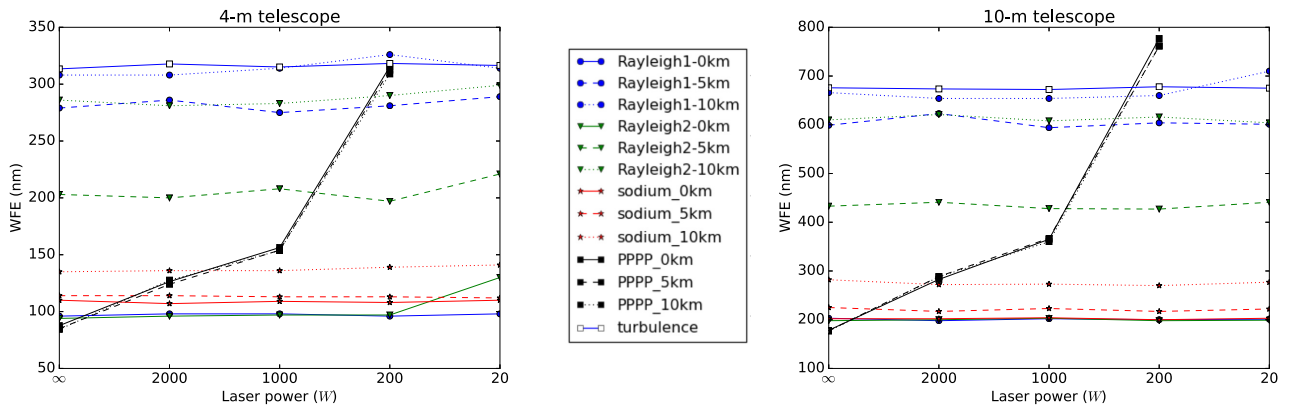$$\sigma^2 = \sum_{i}^{n} \sigma_i^2, \tag{27}$$

Figure 18. Performance of PPPP and SH with Rayleigh and sodium LGSs on 4-m and 10-m telescopes. The *x*-axis is the laser power (where '∞' means infinite power, i.e. without noise). The turbulence layer is located at 0, 5, or 10 km. Rayleigh1 and Rayleigh2 represent 10 and 20 km of Rayleigh scatter height with the laser pulse length 1 and 5 km correspondingly. For the 4-m telescope, the pixel number across the detectors is 32, while for the 10-m telescope it is 80 to keep the pixel size projected to the object plane the same. The result is an average of 100 iterations from *Soapy* simulation. 78 Zernike modes are used for both 4-m and 10-m telescopes as it is easy to compare.

Table 4. WFE (nm) caused by focus anisoplanatism in terms of Rayleigh LGSs focused at 10 and 20 km and sodium LGS when the turbulence layers are located at 5 or 10 km, respectively.

	4-m telescope		10-m telescope	
Turbulence layer	5 km	10 km	5 km	10 km
Rayleigh LGS (10 km)	260	291	559	630
Rayleigh LGS (20 km)	176	268	375	570
Sodium LGS	53	90	63	181

where σ^2 is the total variance and σ_i^2 is the variance of the *i*-th element. Here, the total variance σ^2 is $\sigma_{\rm LGS}^2$, including elements of $\sigma_{\rm NGS}^2$ and $\sigma_{\rm f}^2$ (representing focus anisoplanatism). $\sigma_{\rm LGS}^2$ is shown in Fig. 18 corresponding to ∞ power. $\sigma_{\rm NGS}^2$ can be calculated according to Noll (1975).

$$\Delta_J = 0.2944 \times J^{-\sqrt{3}/2}(D/r_0)^{5/3}({\rm rad}^2) \quad \text{for large } J. \tag{28}$$

So $\sigma_{\rm NGS}$ for 4-m and 10-m telescopes should be

$${\rm WFE}_{\Delta_{78}}(D = 4\,{\rm m}) = 101\,{\rm nm},$$
$${\rm WFE}_{\Delta_{78}}(D = 10\,{\rm m}) = 216\,{\rm nm}, \tag{29}$$

when $r_0 = 0.15$ m at 500 nm. Given $\sigma_{\rm LGS}^2$ and $\sigma_{\rm NGS}^2$, the WFE caused by focus anisoplanatism is calculated and shown in Table 4. We can see that the lower the LGS, the larger the telescope or the higher the turbulence layer is, the bigger the WFE caused by the anisoplanatism becomes.

As for the PPPP results, we can see that the PPPP WFE is very similar no matter whether the turbulence layer is located at 0, 5, or 10 km for both 4-m and 10-m telescopes. That proves PPPP does not suffer from focus anisoplanatism. From another point of view PPPP can achieve ∼100 nm WFE rms for a 4-m telescope and ∼200 nm WFE rms for a 10-m telescope without noise (see Fig. 18), which are very similar to the theoretical results according to equation (29). That means PPPP WFE only comes from the finite DM compensation and demonstrates again that PPPP is a focus-anisoplanatism free method.

However, from Fig. 18, the PPPP WFE increases rapidly when the laser power declines compared with the SH WFS, which indicates that PPPP is more sensitive to the noise than the SH WFS. Particularly when only a 20 W laser is used, the WFE of PPPP is

approximately 1200 nm for a 4-m telescope and 3000 nm for a 10-m telescope. Increasing the SNR of PPPP is of critical importance to advance this new technique to a practical level. Now we are working on a non-linear reconstruction – Neural Network to reduce the laser power requirement. Also, to increase the total laser power for a large telescope, it is not strictly required to use a coherent light for PPPP. So we can simply combine several low-power lasers together with each laser illuminating a small area of the pupil. Regarding the safety issue, PPPP actually wins in this aspect since a broad collimated beam is used instead of a tightly focused laser beam, which concentrates a very large amount of energy near the focus.

Apart from removal of focus anisoplanatism, relief of safety hazards, and its simplicity compared to LTAO, there are other potential benefits regarding PPPP. For example, sodium LGSs vary temporally and spatially, causing measurement biases that appear at all time-scales and lead to a large measurement error from the corresponding LGS WFS (Wang 2015). Also, due to the finite depth of the sodium layer, each sub-aperture of the SH WFS will see an elongated spot, which will also arouse measurement error, and this phenomenon becomes more serious for large telescopes. PPPP, however, will have no such problems, and shows a great potential for ELTs.

5 CONCLUSIONS

We have demonstrated a novel alternative LGS scheme – PPPP and its corresponding wavefront sensing and reconstruction method. We analyse two particular aspects: the PPPP signal and the high-order effect theoretically. A detailed Monte Carlo model including upward propagation, return path, and reconstruction has been carried out. The recommendations that we draw from the simulation include the optimum pixel number to sample the pupil in the detector ($N = 32$), the optimum number of Zernike modes (which is 78), propagation altitudes h_1 and h_2, and the choice for the laser beam modulation (Gaussian beam is better than a top-hat). We also investigate the effect of the height of one turbulence layer and multiple turbulence layers located at different altitudes and find that multiple turbulence layers will not reduce PPPP performance as long as the turbulence layers are below h_1. We present a detailed SNR analysis when photon and read noise are introduced. By integrating PPPP simulation model into a full Monte Carlo end-to-end AO simulation

tool, *Soapy*, we obtain the PPPP performance compared with a conventional SH WFS with a Rayleigh LGS focused at 10 or 20 km, or a sodium LGS for 4-m and 10-m telescopes, respectively. From the *Soapy* simulation results, we can confirm that PPPP does not suffer from focus anisoplanatism.

ACKNOWLEDGEMENTS

REFERENCES

Bouchez A., 2004, Proc. Adv. Adapt. Opt., 5490, 321
Buscher D. F., Love G. D., Myers R. M., 2002, Opt. Lett., 27, 149
Gavel D., Neyman C., 2007, Keck Adaptive Optics Note 475
Goodman J., 1996, Introduction to Fourier Optics, McGraw-Hill, New York
Gureyev T. E., Nugent K. A., 1996, J. Opt. Soc. Am. A, 13, 1670
Hardy J., 1988, Adaptive Optics for Astronomical Telescopes. Oxford Univ. Press, Oxford, UK
Mark Milman D. R., Needels L., 1996, J. Opt. Soc. Am. A, 13, 1226
Noll R. J., 1975, J. Opt. Soc. Am., 66, 207
Reeves A. P., 2015, Laser Guide Star Only Adaptive Optics: The Development of Tools and Algorithms for the Determination of Laser Guide Star Tip-Tilt (Doctoral dissertation), Durham University, Durham, UK
Roddier F., 1988, Appl. Opt., 27, 1223
Schmidt J. D., 2010, Numerical Simulation of Optical Wave Propagation, SPIE Press. Bellingham, USA
Teague M. R., 1983, J. Opt. Soc. Am., 73, 1434
Thompson L. A., Castle R. M., 1992, Opt. Lett., 17, 1485
Tuthill P., 2016, SPIE Astronomical Telescopes + Instrumentation, Edinburgh, UK, 9907,
van Dam M. A., Lane R. G., 2002, J. Opt. Soc. Am. A, 19, 1390
Voelz D., 2011, Computational Fourier Optics. SPIE Press, Bellingham, USA
Wang L., Ellerbroek B., 2015, Proc. Adapt. Opt. Extremely Large Telesc., 4, 1

This paper has been typeset from a TEX/LATEX file prepared by the author.